Comparative Investigation into Fault-Tolerant Dual Three-Phase Permanent Magnet Synchronous Machines with Modular Windings for eVTOL Applications

1st Yuwen Xu
Department of Mechanical Engineering
University College London
London, UK
yuwen.xu.24@ucl.ac.uk

2nd Shun Cai*
Department of Mechanical Engineering
University College London
London, UK
shun.cai@ucl.ac.uk

3rd Mehdi Baghdadi
Department of Mechanical Engineering
University College London
London, UK
m.baghdadi@ucl.ac.uk

4th Zachary Edwards
Department of Mechanical Engineering
University College London
London, UK
zachary.edwards.24@ucl.ac.uk

5th Zeliang Zhang
Power Electronics and Machines Centre
University of Nottingham
Nottingham, UK
Zeliang.Zhang1@nottingham.ac.uk

6th Guangzhao Luo
Research & Development Institute of Northwestern Polytechnical University
Shenzhen, China
guangzhao.luo@nwpu.edu.cn

***Abstract*—High reliability and high-torque-density are paramount for electric vertical take-off and landing (eVTOL) applications. This paper aims to investigate and evaluate the influence of different winding configurations on an interior permanent magnet synchronous machine (IPMSM) under healthy and various fault conditions. In this paper, four sets of dual 3-phase winding configurations, including the conventional overlapped winding, two modular windings, and toroidal winding (TW) are developed to achieve excellent fault-tolerance. Firstly, the winding configurations of all designs are introduced based on the winding function and the magnetomotive force (MMF). Then, the output performance and fault-tolerant performance of the machine with different winding configurations are evaluated. The results indicate that the conventional overlapped winding features the highest output torque, while the modular winding demonstrates the improved fault-tolerant capability. Moreover, the adoption of TW can further enhance the fault-tolerance of the machine while maintaining its output performance despite its complexity in manufacturing.**

Keywords—Dual 3-phase winding, modular winding, toroidal winding, fault-tolerant capabilities

I. Introduction

The aircraft electrification, such as electric vertical take-off and landing (eVTOL) technology has become ever-grown popular in commercial aircraft transport with the target of Net-Zero [1] [2]. In the application of eVTOL, high-torque-density and high reliability are key concerns to ensure the safety and comfort of passengers [3] [4]. The development in magnetic materials allows improvements in the power-density and efficiency of the permanent magnet (PM) machine [5]. However, the high PM flux generated by PMs can also trigger excessive short-circuit (SC) currents. Therefore, the reliability design of the PM machine remains a severe challenge.

The high reliability requirement necessitates the excellent fault-tolerance of the machine. The multi-phase and multiple 3-phase winding have been considered as an effective way to improve the fault-tolerant capability as shown in Fig. 1. They can offer significant advantages by reducing the power rating of each phase, minimizing torque ripple and maximizing torque density [6]-[8]. Moreover, these configurations facilitate a modular winding design, where multiple 3-phase winding groups can be structured into independent modules, as shown in Fig. 2 [9] [10]. Each module consists of multiple 3-phase sub-modules and is driven by a dedicated 3-phase inverter, thereby enhancing the redundancy and fault-tolerance of drive systems.

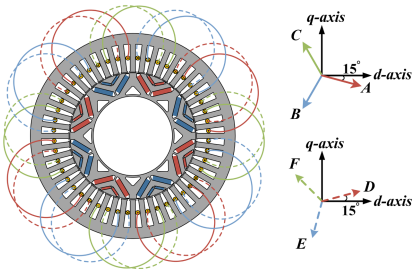

Fig. 1. FT-IPMSM with conventional overlapped winding (W1) and phasor diagrams.

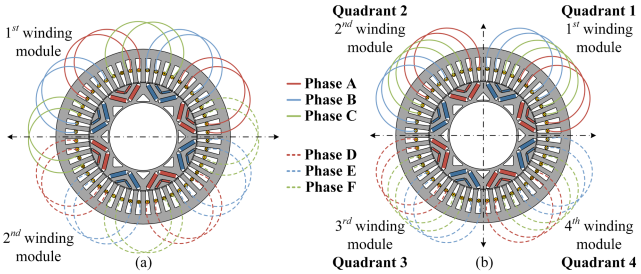

Fig. 2. Modular dual 3-phase winding configurations. (a) Two winding modules (W2), (b) Four winding modules (W3).

To further enhance torque density, fractional-slot concentrated winding (FSCW) has been proposed due to its short end-winding length and high slot filling factor [12]. However, the presence of significant sub-order and super-order harmonics in the air-gap field negatively impacts machine efficiency. In contrast, toroidal winding (TW) offers

multiple advantages: it can not only reduce axial length without compromising output performance, but enhance thermal dissipation through the integration of additional cooling ducts [13]. Furthermore, its relatively high leakage flux helps limit SC currents, which is particularly beneficial for fault-tolerant design. Therefore, TW is considered as a promising candidate for high performance and high reliability operation.

This paper aims to study the fault-tolerant capability of a dual 3-phase 48-slot/8-pole fault-tolerant IPMSM (FT-IPMSM) with different winding configurations. The rest of the article is organized as follows. In section II, four winding configurations, including conventional overlapped winding, two modular windings as well as the TW have been introduced for further analysis. In Section III, the operation performance of the FT-IPMSM with four winding configurations has been evaluated and compared in detail. In this section, the fault-tolerant capability of the machine is evaluated under one-set open-circuit (OC) fault condition and one-set SC fault condition. Finally, the last section concludes the article.

TABLE I. DESIGN SPECIFICATIONS OF THE PROPOSED FT-IPMSM

	Parameter	Value
Structure Parameters	Slot/pole combination	48/8
	Stator outer radius, R_{so} (mm)	181.9
	Stator inner radius, R_{si} (mm)	113.2
	Rotor inner radius, R_{ri} (mm)	65
	Airgap length, g (mm)	0.73
Key Performance	Rated speed, n (r/min)	3000
	Rate torque, T_e (Nm)	130
	Rated current, I_{rms} (A)	107.5
	Efficiency, (%)	96

II. DUAL THREE-PHASE WINDING CONFIGURATION

A. Modular Winding Configuration Designs

The FT-IPMSM analyzed in this study is a 48-slot/8-pole 2-layer V-shaped PM machine, as shown in Fig. 1. The slot/pole combination is chosen with a consideration of the overall complexity and redundancy of the proposed design [10]. Moreover, the 2-layer V-shaped rotor topology has been adopted to improve the torque density. The design specifications of the machine are shown in TABLE I.

As shown in Fig. 1, in conventional overlapped dual 3-phase winding, denoted as W1, two sets of 3-phase winding are bundled with each other and the angle displacement of two winding sets is 30°. The magnetomotive force (MMF) generated by each set of 3-phase winding can be expressed as

$$\mathrm{MMF}_1(\alpha) = \sum_{k=A,B,C} N_k(\alpha) i_k \tag{1}$$

$$N_k(\alpha) = n_k(\alpha) - \langle n_k(\alpha) \rangle \tag{2}$$

where, $\mathrm{MMF}_1(\alpha)$ is the MMF generated by the ABC set, i_k is the current in phase k, $N_k(\alpha)$ and $n_k(\alpha)$ are the winding function and turn function of coil k, respectively, $\langle n_k(\alpha) \rangle$ is the average value of turn function [11].

Under the healthy condition, the MMF generated by the ABC winding in W1 is shown in Fig. 3. It can be discovered that the MMF waveform contains only the ac component $F_{ac}^{W1,1}$, which can be calculated as

$$F_{ac}^{W1,1}(\phi) = \sum_{\nu \in \boldsymbol{O}^*} F_{acv}^{W1,1} \cos(4\upsilon\phi + \varphi_\upsilon) \tag{3}$$

where, $F_{acv}^{W1,1}$ and φ_ν are the amplitude and phase of the ν^{th} MMF harmonic, respectively, ν belongs to the positive odd integer set $\boldsymbol{O}^*$.

As shown in Fig. 3, the MMF generated by each set of 3-phase winding spread over the entire air-gap from 0° to 360°, thereby resulting in a significant magnetic coupling between two winding sets.

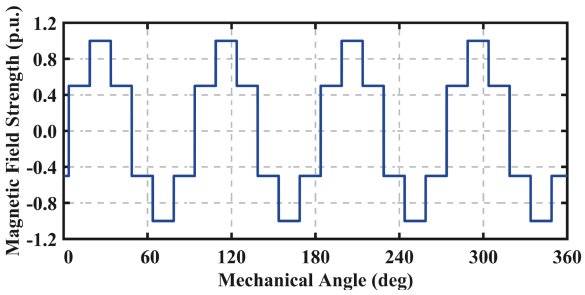

Fig. 3. MMF generated by ABC set in W1.

To construct modular windings, there are two approaches that can be employed to rewind W1. One method involves reconfiguring W1 into two modules, each occupying half of the machine space, denoted as W2, as shown in Fig. 2(a). The MMF generated by the ABC set in W2 can be calculated based on (1) and (2). The corresponding MMF waveform is depicted in Fig. 4. It can be observed that the MMF contains only ac component. However, a portion of the MMF waveform is coupled by the DEF set and the resultant waveform loses its symmetry due to the physical and magnetic coupling between two winding sets, introducing significant harmonics in the MMF spectrum, as shown in Fig. 4(a).

Alternatively, W1 can also be divided into four modules, each occupying one-quarter of stator slots (referred to as W3) as shown in Fig. 2(b). In W3, two of 3-phase sub-modules are connected to one 3-phase inverter when considering the dual 3-phase design, i.e. the 1st and 2nd winding modules belong to the ABC set, while the remaining belong to the DEF set. The proposed segregated modular winding can realize an effective electric and thermal isolation between ABC set and DEF set. However, the magnetic coupling cannot be eliminated. The MMF generated by ABC set in W3 is shown in Fig. 4(b). It can be discovered that the resultant MMF waveform contains both ac component and offset component. The general expression of the resultant MMF can be derived as [9]

$$\begin{aligned} F_a^{W3,1}(\phi,t) &= \begin{cases} F_{ac}^{W3,1}(\phi,t) + F_{os}^{W3,11}(\phi,t) \\ F_{os}^{W3,21}(\phi,t) \end{cases} \\ F_{ac}^{W3,1} &= \sum_{\nu \in \boldsymbol{O}^*} F_{acv}^{W3,1} \cos(4\upsilon\phi + \psi_\upsilon) \\ F_{os}^{W3,11} &= \frac{1}{2}(N_A i_A + N_B i_B - N_C i_C) \\ F_{os}^{W3,21} &= -F_{os}^{W3,11} \end{aligned} \tag{4}$$

where, $F_a^{W3,1}$ is the resultant MMF generated by ABC set, $F_{ac}^{W3,1}$, $F_{acv}^{W3,1}$, and ψ_ν are the ac component and the amplitude and phase of the ν^{th} harmonic, respectively, $F_{os}^{W3,11}$ and $F_{os}^{W3,21}$ are the offset components over the ABC region and DEF region, respectively.

As shown in (4) and Fig. 4(b), the MMF ac component exists only in the ABC set region, while the offset component spans the entire air-gap. It further reflects that different sets of 3-phase winding coupled with each other through the MMF offset component in W3.

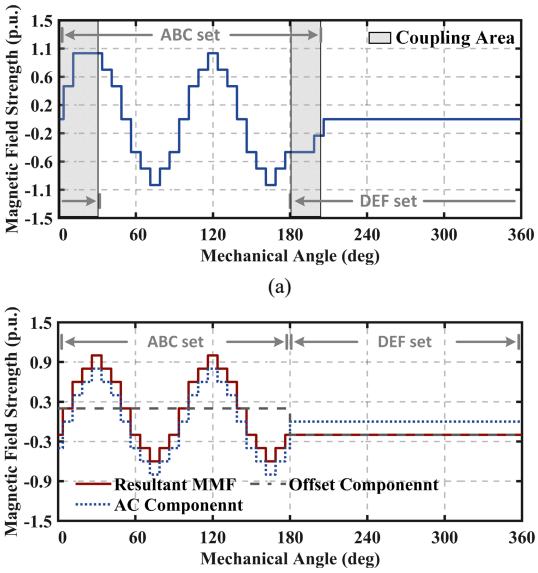

Fig. 4. MMF generated by two modular winding configurations. (a) MMF generated by ABC set in W2, (b) MMF generated by ABC set in W3.

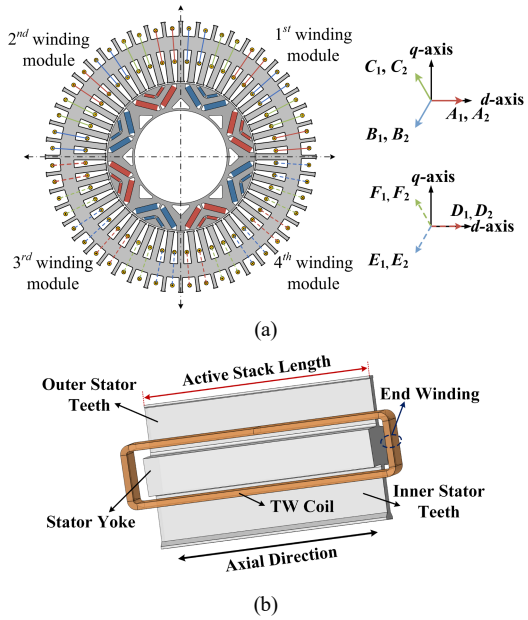

Fig. 5. Cross-section of FT-IPMSM with TW. (a) Winding configurations, (b) Coil schematic.

B. *Toroidal Winding Design*

The TW configuration, which features short end-winding length and flexible installation, has been widely discussed in some applications where axial length and torque density are of key importance. The cross-section of the FT-IPMSM equipped with TW and its corresponding coil schematic are shown in Fig. 5.

In this article, the TW also adopts the modular dual 3-phase winding configuration, as shown in Fig. 5(a). The operational performance and fault-tolerant capability of the TW machine will be investigated and compared to the W1–W3 in the next section.

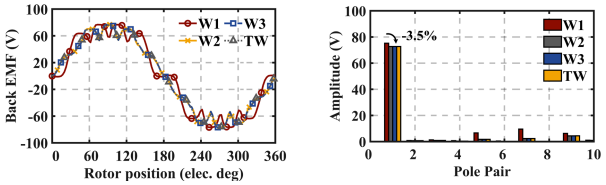

Fig. 6. Comparison of back EMFs. (a) Back EMF waveforms, (b) Back EMF spectrum.

TABLE II. WINDING FACTOR FOR FOUR WINDING CONFIGURATIONS

$k_{dp\nu}$	W1	W2	W3	TW
$\nu = 1$	1	0.967	0.967	0.967
$\nu = 5$	1	0.707	0.707	0.707

III. PERFORMANCE COMPARISON OF FT-IPMSM

In this section, the operation performance of the prototype with different winding configurations has been investigated and evaluated under healthy and various fault conditions, including the one-set OC fault condition and the one-set SC fault condition. All evaluations are conducted at the rated speed of 3000r/min. It should be noted that faults are always considered to occur in the ABC set unless otherwise specified.

A. *Healthy Condition*

The performance of the machine under healthy condition is analyzed first, as this represents the predominant state of operation. The back electromotive force (EMF) waveforms and spectrums of the proposed four winding designs are shown in Fig. 6. It can be observed that W1 has the highest fundamental back-EMF among the four designs due to the higher fundamental winding factor. The fundamental and dominant harmonic winding factor (i.e. the 5^{th} harmonic) for each winding design are listed in TABLE II. It can be discovered that W1 demonstrates a relatively weaker harmonic suppression capability compared to other designs. Consequently, its total harmonic distortion (THD) is approximately 0.26%, which is higher than that of the W2, W3, and TW (0.16%).

For each winding case, two sets of 3-phase winding are injected with 3-phase currents. Therefore, the resultant torque waveforms for all winding designs are shown in Fig. 7. It is shown that W1 demonstrates the highest output torque with about 130Nm, followed by W2 and W3 with a value of 123Nm. The TW has the lowest average torque, around 122Nm, due to the additional flux leakage caused by the coils beyond the stator yoke. The superior output torque of the W1 can be attributed to its highest fundamental winding factor and the 30° phase shift between the excited currents of two winding sets.

In addition, it can be discovered that the dominant torque pulsation harmonic of W1 is the $12f_e$ (f_e is electrical frequency) harmonic as shown in Fig. 7. In contrast, both $6f_e$ and $12f_e$ torque ripple components are observed in the torque waveforms of W2, W3, and TW as shown in Fig. 7. The absence of the $6f_e$ torque ripple component in W1 can be explained by the torque contributions of each winding set. For W1, the torque ripple component generated by each set of 3-phase winding can be deduced as

$$T_{ripple}^{k} = -\frac{p}{2}\frac{\mu_0}{g} r_g l_{stk} \pi \cdot \sum_{\substack{h=6\nu\mp1 \\ \nu=1,2,3}} \left(h F_{a,h}^{k} F_{pm,h} \sin\left((h \pm 1)\omega_e t \pm \eta\right)\right) \quad (5)$$

where, $F_{pm,h}$ is the amplitude of the h^{th} PM harmonic, $F_{a,h}^{k}$ is the amplitude of the h^{th} armature harmonic generated by the of winding set k (k = 1 and 2, representing ABC set or DEF set, respectively), η is the phase of torque ripple, ω_e is the electrical rotor speed. In W1, the armature MMF generated by each set of 3-phase winding can be expressed as

$$F_a^1 = \sum_{i \in \boldsymbol{O}^*} F_{a,i}^1 \sin\left(2i\phi + \omega_e t + \varphi_a\right) \quad (6)$$

and

$$F_a^2 = \sum_{i \in \boldsymbol{O}^*} F_{a,i}^2 \sin\left(2i\phi + \omega_e t + \varphi_a - 30^\circ\right) \quad (7)$$

where, $F_{a,i}$ is the amplitude of the i^{th} armature MMF harmonic, φ_a is the phase of armature MMF, i belongs to the positive odd integer set $\boldsymbol{O}^*$.

From (6) and (7), it is shown that the MMF generated by two winding sets are out of phase of 30°. Therefore, the $6f_e$ torque fluctuation component generated by two sets of 3-phase winding has a 180° displacement, which can be calculated by substituting (6) and (7) into (5) as

$$T_{ripple}^{1} = -\frac{p}{2}\frac{\mu_0}{g} r_g l_{stz} \pi \left(h f_{s,h}^{1} f_{r,h} \sin\left(6\omega_e t \pm \eta\right)\right) \quad (8)$$

and

$$T_{ripple}^{2} = -\frac{p}{2}\frac{\mu_0}{g} r_g l_{stz} \pi \cdot h f_{s,h}^{2} f_{r,h} \sin\left(6\omega_e t \pm \eta - 180^\circ\right) \quad (9)$$

Consequently, these components counteract each other, eliminating the $6f_e$ torque ripple in the resultant torque. However, the $6f_e$ torque ripple component cannot be mitigated in W2, W3, and TW as the torque contributions from the two winding sets are in phase.

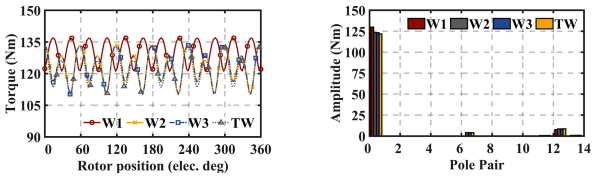

(a) (b)

Fig. 7. Comparison of torque under healthy condition. (a) Torque waveforms, (b) Torque spectrum.

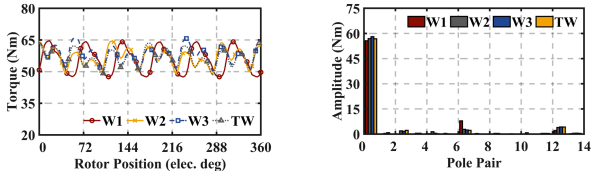

(a) (b)

Fig. 8. Comparison of torque under OC fault condition. (a) Torque waveforms, (b) Torque spectrum.

B. One-Set OC Fault Condition

The continuous working capability under the OC condition is an essential indicator for evaluating the fault-tolerance of the machine. Therefore, the operation performance of the machine under the one-set OC fault condition will be investigated in this section.

In OC cases, the 3-phase inverter of the faulty set should be deactivated while the healthy set is still excited with 3-phase healthy currents. In this condition, the resultant torque waveforms are shown in Fig. 8. It can be observed that the output torque in all cases is slightly less than half of that in the healthy condition, with W3 exhibiting the highest output torque, followed by TW. Moreover, all cases exhibit a distinct $6f_e$ torque fluctuation component in the resultant waveform, which is attributed to the 5^{th} and 7^{th} MMF harmonic generated by the DEF winding.

It is worth noting that the W2, W3, and TW also show a $2f_e$ torque ripple component in the resultant torque waveform, as shown in Fig. 8. It can be attributed to the periodic saturation in stator iron.

C. One-Set SC Fault Condition

The SC fault performance evaluation is carried out based on the most severe condition, i.e. the one-set SC condition. As we assume the fault occurs in the ABC set, the inverter of the ABC set should be turned off to form the terminal short-circuit (TSC), while the DEF set is still excited with 3-phase currents. The predicted SC currents of each winding case are shown in Fig. 9.

It is shown that the 3-phase currents can no longer remain symmetry under the SC condition and the rms value of phase B is always higher than that of phase A and phase C for all winding designs. Among all winding designs, W1 shows the highest SC currents compared with other winding cases, which is about 1.46 times the rated value. In contrast, the SC currents in W2–W3 are comparable, reaching around 1.15p.u., followed by TW whose SC currents are lowest at nearly 1.12p.u. The reason why SC currents vary from each winding design can be explained by the equivalent voltage equation as

$$\begin{bmatrix}0\\0\end{bmatrix} = \begin{bmatrix}R & -\omega_e L_{q1q1}\\ \omega_e L_{d1d1} & R\end{bmatrix}\begin{bmatrix}I_{d1}(t)\\ I_{q1}(t)\end{bmatrix} + \begin{bmatrix}L_{d1d1} & 0\\ 0 & L_{q1q1}\end{bmatrix}\cdot\frac{d}{dt}\begin{bmatrix}I_{d1}(t)\\ I_{q1}(t)\end{bmatrix} + \begin{bmatrix}0\\ \omega_e\psi_{\mathrm{PM}}\end{bmatrix} + \omega_e\begin{bmatrix}-L_{q2q1}I_{q2}\\ L_{q2d1}I_{q2}\end{bmatrix} \quad (10)$$

where, $I_{d1}(t)$ and $I_{q1}(t)$ are d-axis and q-axis SC currents, R is the phase resistor, L_{d1d1} and L_{q1q1} are the self-inductance in the dq plane, respectively.

When ignoring the phase resistor R, the d-axis and q-axis SC currents can be obtained by solving (10)

$$I_{d1}(t) = -\frac{\psi_{PM} + L_{q2d1}I_{q2}}{L_{d1d1}} \quad (11)$$

$$I_{q1}(t) = -\frac{L_{q2q1}I_{q2}}{L_{q1q1}} \quad (12)$$

From (11) and (12), it can be concluded that the SC currents are mainly related to the PM flux, self-inductances (L_{d1d1}, L_{q1q1}) and mutual inductance (L_{q2d1}). The inductances of the proposed machine with different winding designs are shown in Fig. 10. It can be discovered that W1 demonstrates a significantly lower self-inductance (L_{d1d1}, L_{q1q1}) compared to

W2 and W3. Meanwhile, the PM flux of W1 is the highest among the three winding configurations despite its relatively lower mutual inductance (L_{q2d1}), contributing to the largest *d*-axis flux in SC windings. In this condition, W1 exhibits the highest SC currents among all winding designs, followed by W2 and W3. It should be noted that the SC currents of TW prototype are further reduced compared to that of W3, owing to higher self-inductance induced by increased leakage flux.

The predicted SC torque is depicted in Fig. 11. As can be observed, there is a significant reduction in the average torque in W1 under the SC condition due to the magnetic coupling between two sets of 3-phase winding. When the fault occurs, SC currents generated by fault winding have a demagnetization effect, which will diminish the flux generated by the healthy set, as shown in Fig. 12(a). In comparison, it is shown that the flux generated by the healthy winding can be maintained in W3 due to the modular winding design, as shown in Fig. 12(b). Therefore, the average torque of W3 is much larger than that of W1, reaching around 58Nm, which is slightly lower than half of that under healthy condition. The conclusions can also be applied to W2 and TW. Furthermore, the average torque of TW design is the highest under the SC fault due to the lowest SC currents.

Additionally, a relatively high $2f_e$ torque fluctuation component can be observed in the SC torque of both W3 and TW as shown in Fig. 11. The $2f_e$ torque component can be attributed to the negative sequence component in flux linkages of the SC winding. The negative sequence flux linkage induces $2f_e$ fluctuation in *q*-axis SC currents, further resulting in the $2f_e$ fluctuation in the resultant torque.

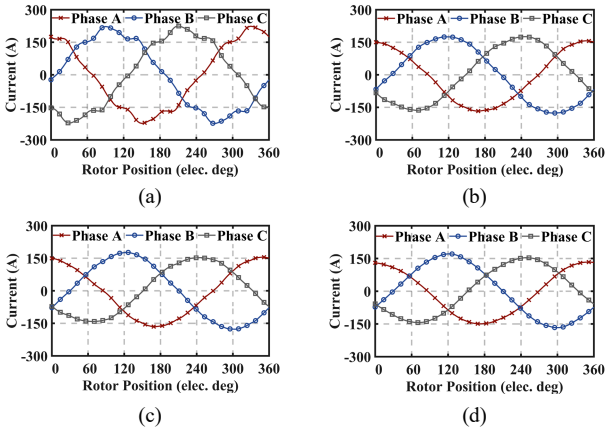

Fig. 9. SC currents comparison. (a) W1, (b) W2, (c) W3, (d) TW.

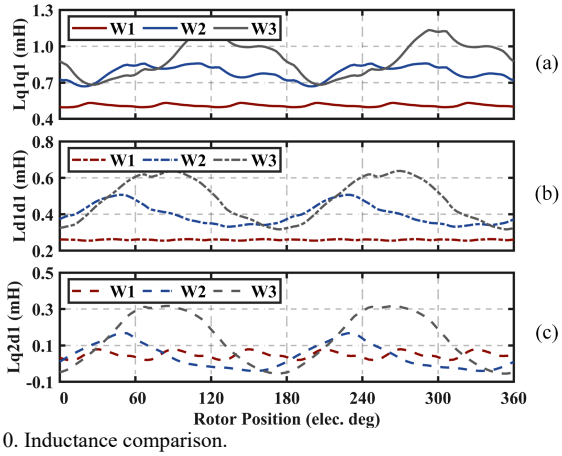

Fig. 10. Inductance comparison.

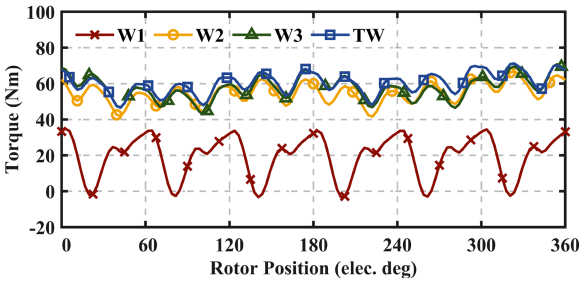

Fig. 11. SC torque comparison.

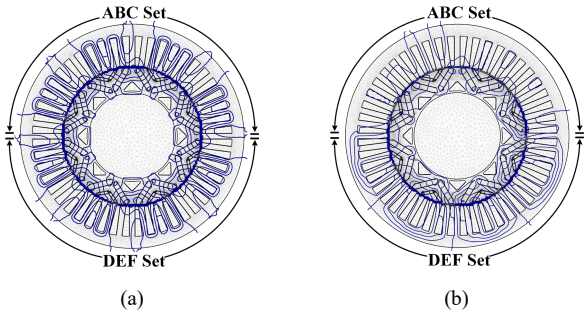

Fig. 12. Flux lines distribution. (a) W1, (b) W3.

IV. Conclusions

This paper investigates the application of four different winding configurations for a dual 3-phase 48-slot/8-pole FT-IPMSM. The electromagnetic performance has been analyzed and compared in-depth under healthy and different faulty conditions. The results indicate that the conventional overlapped winding demonstrates the best output performance under the healthy condition. Moreover, all winding configurations have comparable performance under the OC fault. Additionally, two modular windings and TW demonstrate higher output torque and lower SC currents under the SC fault condition. The results further prove that the application of modular windings can enhance the fault-tolerant capability of the machine. It should also be mentioned that TW has limited improvement in the performance of the prototype but needs additional stator slots to adopt coils, which complicates the manufacturing process.

Acknowledgment

This work was supported by Shenzhen Science and Technology Program under Grant GJHZ20240218114402006, and in part by Royal Society under Grant RG\R1\251550.

References

[1] C. Gerada, M. Galea and A. Kladas, "Electrical machines for aerospace applications," *2015 IEEE Workshop on Electrical Machines Design, Control and Diagnosis (WEMDCD)*, Turin, Italy, 2015, pp. 79-84.

[2] B. Sarlioglu and C. T. Morris, "More Electric Aircraft: Review, Challenges, and Opportunities for Commercial Transport Aircraft," *IEEE Trans. Transp. Electrif.*, vol. 1, no. 1, pp. 54-64, June 2015.

[3] N. Dave et al., "Fast Sizing Tool and Optimization Technique for Concentrated Wound Slotless Outer Rotor Motor for eVTOL Application," *2022 International Conference on Electrical Machines (ICEM)*, Valencia, Spain, 2022, pp. 2094-2099.

[4] W. Cao, B. C. Mecrow, G. J. Atkinson, J. W. Bennett and D. J. Atkinson, "Overview of Electric Motor Technologies Used for More Electric Aircraft (MEA)," *IEEE Trans. Ind. Electron.*, vol. 59, no. 9, pp. 3523-3531, Sept. 2012.

[5] Z. Q. Zhu and D. Howe, "Electrical Machines and Drives for Electric, Hybrid, and Fuel Cell Vehicles," *Proc. IEEE*, vol. 95, no. 4, pp. 746-765, April 2007.

[6] F. Wu, P. Zheng, Y. Sui, B. Yu and P. Wang, "Design and Experimental Verification of a Short-Circuit Proof Six-Phase Permanent Magnet Machine for Safety Critical Applications," *IEEE Trans. Magn.*, vol. 50, no. 11, pp. 1-4, Nov. 2014.

[7] N. Bianchi, S. Bolognani and M. D. PrÉDai Pre, "Impact of Stator Winding of a Five-Phase Permanent-Magnet Motor on Postfault Operations," *IEEE Trans. Ind. Electron.*, vol. 55, no. 5, pp. 1978-1987, May 2008.

[8] M. Barcaro, N. Bianchi and F. Magnussen, "Analysis and Tests of a Dual Three-Phase 12-Slot 10-Pole Permanent-Magnet Motor," *IEEE Trans. Ind. Appl.*, vol. 46, no. 6, pp. 2355-2362, Nov.-Dec. 2010.

[9] B. Wang, C. Zha, Y. Xu, J. Wang, M. Cheng and W. Hua, "Comparative Study on Fault-Tolerant Triple Three-Phase PM Machine Drive With Five Modular Windings," *IEEE Trans. Ind. Electron.*, vol. 70, no. 10, pp. 9720-9730, Oct. 2023.

[10] B. Wang, J. Wang, B. Sen, A. Griffo, Z. Sun and E. Chong, "A Fault-Tolerant Machine Drive Based on Permanent Magnet-Assisted Synchronous Reluctance Machine," *IEEE Trans. Ind. Appl.*, vol. 54, no. 2, pp. 1349-1359, Mar.-Apr. 2018.

[11] Faiz, J. and I. Tabatabaei. "Extension of winding function theory for nonuniform air gap in electric machinery." *IEEE Trans. Magn.*, 38(6): 3654-3657.

[12] F. Wu, C. Tong, Y. Sui, L. Cheng and P. Zheng, "Influence of Third Harmonic Back EMF on Modeling and Remediation of Winding Short Circuit in a Multiphase PM Machine With FSCWs," *IEEE Trans. Ind. Electron.*, vol. 63, no. 10, pp. 6031-6041, Oct. 2016.

[13] H. Li, Z. Q. Zhu and H. Hua, "Comparative Analysis of Flux Reversal Permanent Magnet Machines With Toroidal and Concentrated Windings," *IEEE Trans. Ind. Electron.*, vol. 67, no. 7, pp. 5278-5290, July 2020.

[14] A. Borisavljevic, S. Jumayev and E. Lomonova, "Toroidally-wound permanent magnet machines in high-speed applications," *2014 International Conference on Electrical Machines (ICEM)*, Berlin, Germany, 2014, pp. 2588-2593.